

In-situ deposited multi-layered thin films for lithium-ion batteries

K. Chen, W. Xia, Li Xiang*, Li He, C. Wang, K. Jia, Essam, Li Li, Xi Gao, T. P. Jijf, Li Li, f Li, s W, K. Jia, Essam, Li Li, Xi Gao, T. P. Jijf

Gemological Institute, China University of Geosciences, Wuhan 430074, PR China
 Hubei Gem and Jewelry Engineering Technology Research Center, Wuhan 430074, PR China
 School of Materials Science and Engineering, Huazhong University of Science and Technology, Wuhan 430074, PR China
 Mechanical Engineering, University of Birmingham, Birmingham B15 2TT, UK
 School of Electrical and Electronic Engineering, Huazhong University of Science and Technology, Wuhan 430074, PR China
^fWMG, Materials Engineering Centre, University of Warwick, CV4 7AL Coventry, UK

ARTICLE INFO

Keywords:

Thin film
 Composite
 Sintering
 Coating
 Electrode

ABSTRACT

Conductivity, thin film (3DG) fabrication, multi-layered thin film, composite, sintering, lithium-ion battery, electrochemical performance, surface area, scanning electron microscopy (SEM), atomic force microscopy (AFM), scanning tunneling microscopy (STM), transmission electron microscopy (TEM), X-ray diffraction (XRD), energy-dispersive X-ray (EDS), Fourier transform infrared spectroscopy (FTIR), cyclic voltammetry (CV), electrochemical impedance spectroscopy (EIS), rate capability, cycle life, thermal stability, mechanical stability, environmental stability, etc.

1. Introduction

Graphene, a 2D layered carbon structure, has attracted great attention due to its excellent electrical, mechanical, and thermal properties [1]. Graphene has a theoretical carrier mobility of $2 \times 10^5 \text{ cm}^2 \text{ V}^{-1} \text{ s}^{-1}$ and a thermal conductivity of $\sim 5000 \text{ W m}^{-1} \text{ K}^{-1}$ [2]. However, the large band gap of graphene (2 eV) makes it an insulator. To overcome this problem, various functional groups have been introduced to the graphene surface [3]. After the functionalization, the electrical conductivity of graphene is significantly reduced [4]. The 3D graphene structure, such as graphene aerogel, has a porosity of $\sim 99.7\%$, a surface area of $\sim 0.6 \times 10^3 \text{ m}^2 \text{ g}^{-1}$ [5]. The porous structure of graphene aerogel can significantly reduce the resistance of the electrode.

(2DG), thin film synthesis [5], systems [6,7], synthesis [4], electrochemical performance (EMI) stability [8] etc. Various surface areas of 3DG thin film [9], yield [10], surface area [11], density [12] etc. However, the functional groups still remain on the surface. For example, the oxygen-containing functional groups [13]. Surface area [14]. Density [15]. Most of the systems [16]. By the way, the electrochemical performance, stability, etc. The electrochemical performance of the thin film is significantly reduced compared with the bulk material.

*Corresponding author. Gemological Institute, China University of Geosciences, Wuhan 430074, PR China.
 E-mail address: yxia@cug.edu.cn (Y. Xia).

...t lyst. T... i es e i... t isti s (i., e esitie... i e-
st t), t t t i i fl e t fi l i est t
(i., l y t i ss, f ts) of t 3DG. B si s, t -
t 3DG i i i t t e e t i s f e t t l t l t
(i., e esity, e si s, f lity). H e, est of t e es
t l t l t s y e t i e l t e s i ffi lty
ie sly l t i e esity, fe i st, t e i l Ni fe
lly st e esity y e l y e t e l fe i t
e t t, t s s tly e t i 3DG s e s e e t e l e f e-
s e i i e s e i f t s f e s i f i f t i e l s i 17,18].
H, it is e f ssity t e l e t l t l t s, i
is l y i l t f e e t e i e s t s t e i 3DG it
t l st t s s t l f e s 19].

S l t i l s l t i (SLM), s i e t i i t i -
f t i (AM) t e l e y, is t i l y s i f e t f i t i e
e f s e l s t i t / e i s t - i s i e l (3D) t l t l t s
i t t t s e f e l i t y i s i, f f i i y i e t i e
f l i lity of *in-situ* f t i i lity. T e t, e s
s s e t SLM e e s s t t s e f T i l l e y s 20],
s t i l s s l l e y s 21], N i l l e y s 22]. C i s t e s t i l y s f e l /
s s t t f e l - s y t s i i s t t - e f - t - t -
s i s t i l s. C e i t N i e e t s s t t,
e i s s e s i l s s t t f e e t
i CVD t e t l e e s t t i e l l (< 0.001 t.%)
e t e s s s l f - l i t i e f e, i t t e t i -
lity s i l l y i t l s 23]. W i l N i s
i e s e l i lity (> 0.1 t.%) 17], t i f i l s t
t e f e s e f s s i e i t i e 24]. H e, -
s i SLM e f e i s s t i l l i t s i f y s e f i s f f i i t
t i f e e s l t i i f e i t s i t i s i i t l
e t i lity f l t i lity t e s e e l s l t
(1000–1100). F i t i e e f i s e s e s f f e l s
i SLM is s t i l l f i y l l s 25].

T e e e l i t t i e s, f e t f i s t t i e e s
f s i l e t t e - e t e e 3DG/ e (3DG/C) s t -
t s i SLM s i l t e sly i e i t i e i t CVD e t e f
. A l l - s i y e i - t y e e s e t l t s
i i t i lly i s t i t i SLM f e i e s t t l e l t i e t e -
e s e i f e, s i lly i t s t t e i s e t e y i 9.8(s.3(i e l t i e 445.3, e . l t .2)-3)-412.1(e)-414.6(t i lity)-840.8 j/T1T (I

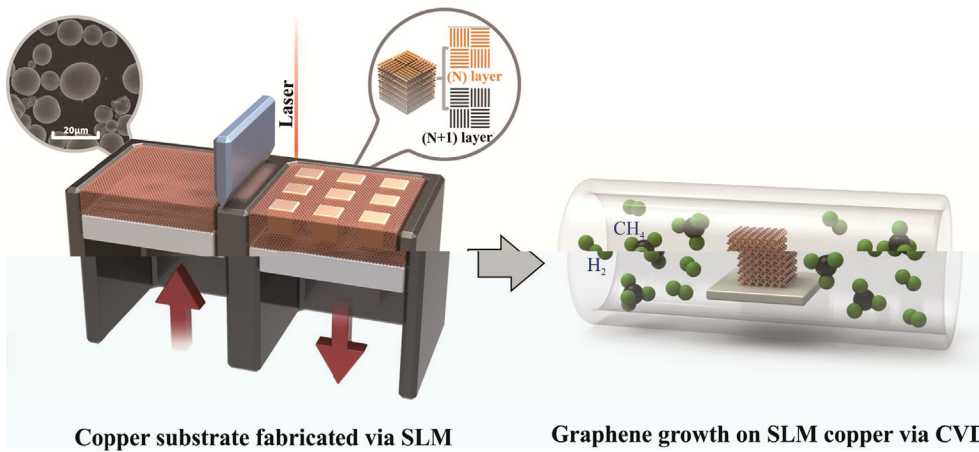


Fig. 1. Illustration of the 3DG/C porous substrate fabrication process followed by *in-situ* CVD for graphene growth on SLM copper substrate.

ASTM B193-2002 and ISO 10361-2:2003 for mechanical properties. The porosity of the porous substrate is $(2 \times 10^{-3} - 5 \times 10^{-3})$ following ASTM E1461-2013 test method for the permeability coefficient (LFA (Laser Flash Analysis, Netzsch LFA457, Germany). Results are given in Table 1 (SENTERRA, B., & GUYON, S. Sintering of 3DG/C porous substrate at 514 °C. *Thin Solid Films* (S11–S21) 2018). The sintering rate is 10 °C/min (VNA, Avia PNA-N5244A, US) with a frequency of 2–18 GHz. The surface area is measured by BET method, and the surface area is given in Table 1.

3. Results and discussion

3.1. Formation of SLM copper

3.1.1. SLM manufacturing of copper under different line energy densities

The test results are shown in Table 1. Different scanning speeds and laser powers were used to fabricate the porous substrate.

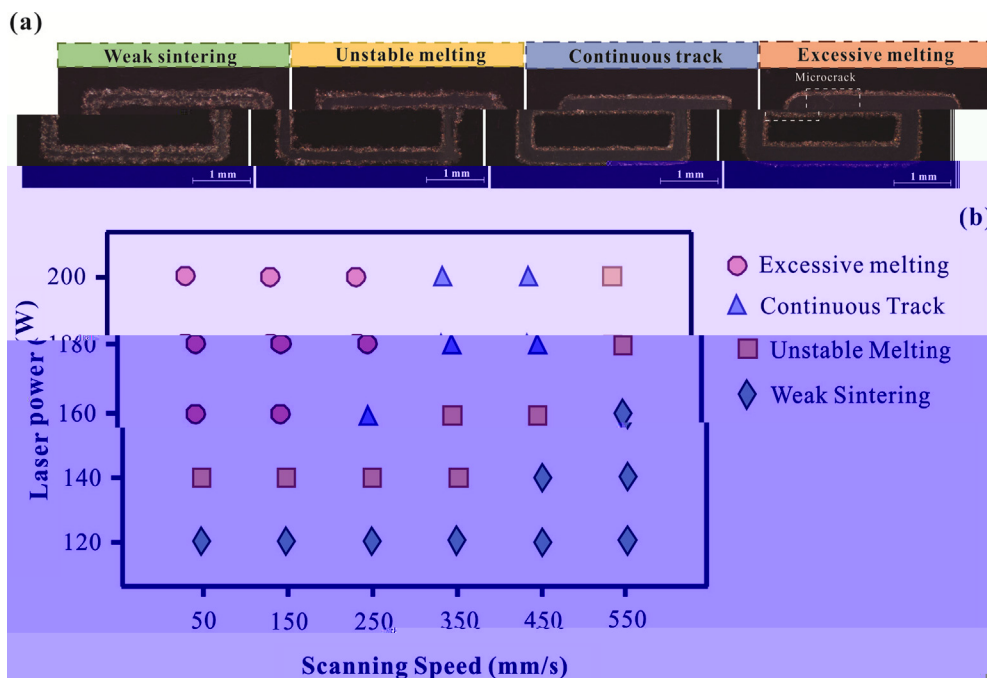


Fig. 2. (a) Typical morphology of porous substrate under different conditions: (a) Weak sintering; (b) Unstable melting; (c) Continuous track; (d) Excessive melting. (b) Laser power vs scanning speed. (For interpretation of the references to this figure legend, the reader is referred to the web version of this article.)

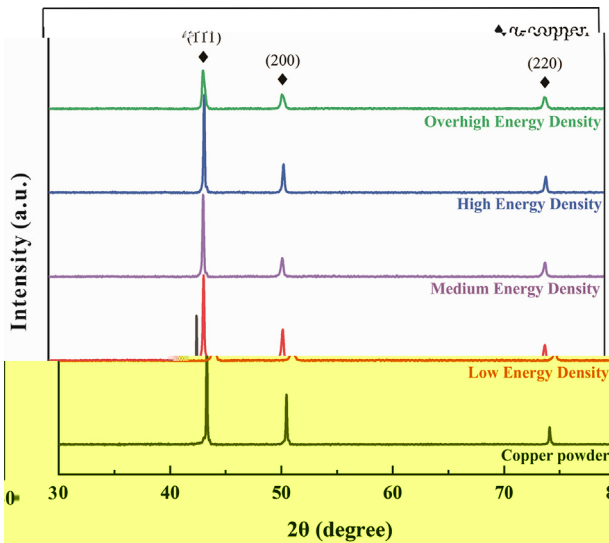


Fig. 3. XRD patterns of copper powder at different energy densities. (For interpretation of the references to colour in this figure legend, the reader is referred to the web version of this article.)

3.1.2. Formation of anisotropic microstructure under different volumetric energy density

The XRD patterns of copper powder at different energy densities are shown in Fig. 3. The (111) and (200) peaks are observed at $2\theta = 43.32^\circ$ and $2\theta = 50.45^\circ$, respectively (Fig. 3). The (111) peak is the most intense. The XRD patterns of copper powder at different energy densities are shown in Fig. 3. The (111) and (200) peaks are observed at $2\theta = 43.32^\circ$ and $2\theta = 50.45^\circ$, respectively (Fig. 3). The (111) peak is the most intense. The XRD patterns of copper powder at different energy densities are shown in Fig. 3. The (111) and (200) peaks are observed at $2\theta = 43.32^\circ$ and $2\theta = 50.45^\circ$, respectively (Fig. 3). The (111) peak is the most intense.

The XRD patterns of copper powder at different energy densities are shown in Fig. 3. The (111) and (200) peaks are observed at $2\theta = 43.32^\circ$ and $2\theta = 50.45^\circ$, respectively (Fig. 3). The (111) peak is the most intense. The XRD patterns of copper powder at different energy densities are shown in Fig. 3. The (111) and (200) peaks are observed at $2\theta = 43.32^\circ$ and $2\theta = 50.45^\circ$, respectively (Fig. 3). The (111) peak is the most intense.

The XRD patterns of copper powder at different energy densities are shown in Fig. 3. The (111) and (200) peaks are observed at $2\theta = 43.32^\circ$ and $2\theta = 50.45^\circ$, respectively (Fig. 3). The (111) peak is the most intense. The XRD patterns of copper powder at different energy densities are shown in Fig. 3. The (111) and (200) peaks are observed at $2\theta = 43.32^\circ$ and $2\theta = 50.45^\circ$, respectively (Fig. 3). The (111) peak is the most intense. The XRD patterns of copper powder at different energy densities are shown in Fig. 3. The (111) and (200) peaks are observed at $2\theta = 43.32^\circ$ and $2\theta = 50.45^\circ$, respectively (Fig. 3). The (111) peak is the most intense.

The XRD patterns of copper powder at different energy densities are shown in Fig. 3. The (111) and (200) peaks are observed at $2\theta = 43.32^\circ$ and $2\theta = 50.45^\circ$, respectively (Fig. 3). The (111) peak is the most intense. The XRD patterns of copper powder at different energy densities are shown in Fig. 3. The (111) and (200) peaks are observed at $2\theta = 43.32^\circ$ and $2\theta = 50.45^\circ$, respectively (Fig. 3). The (111) peak is the most intense.

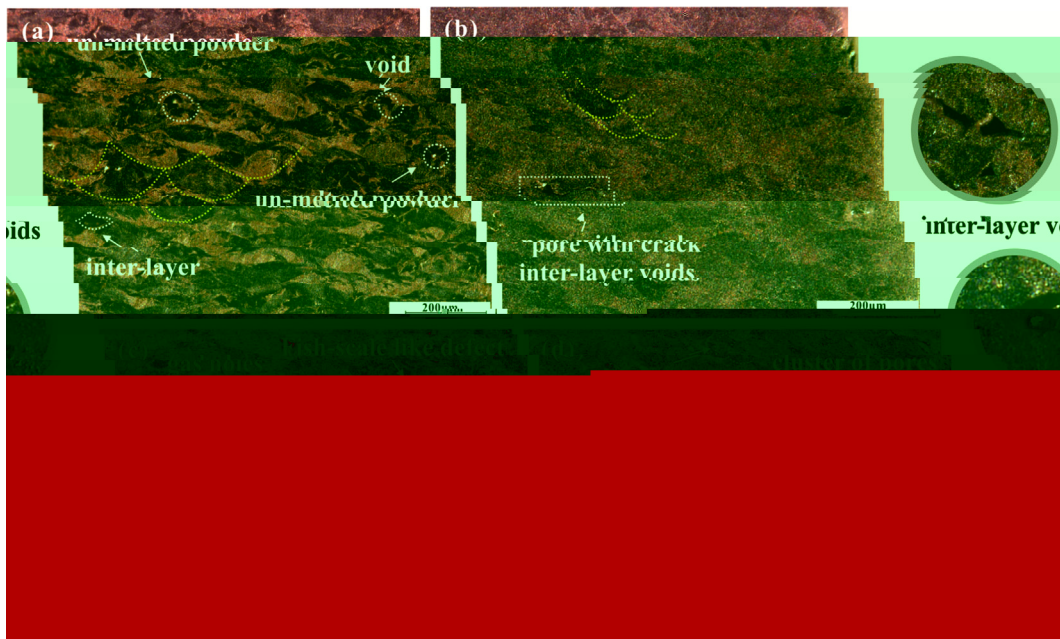


Fig. 4. Optical micrographs of copper powder at different energy densities: (a) 3000 J/cm³, (b) 857 J/cm³, (c) 285 J/cm³, (d) 128 J/cm³, respectively. (For interpretation of the references to colour in this figure legend, the reader is referred to the web version of this article.)

t i t e t e t s e i e i e t.

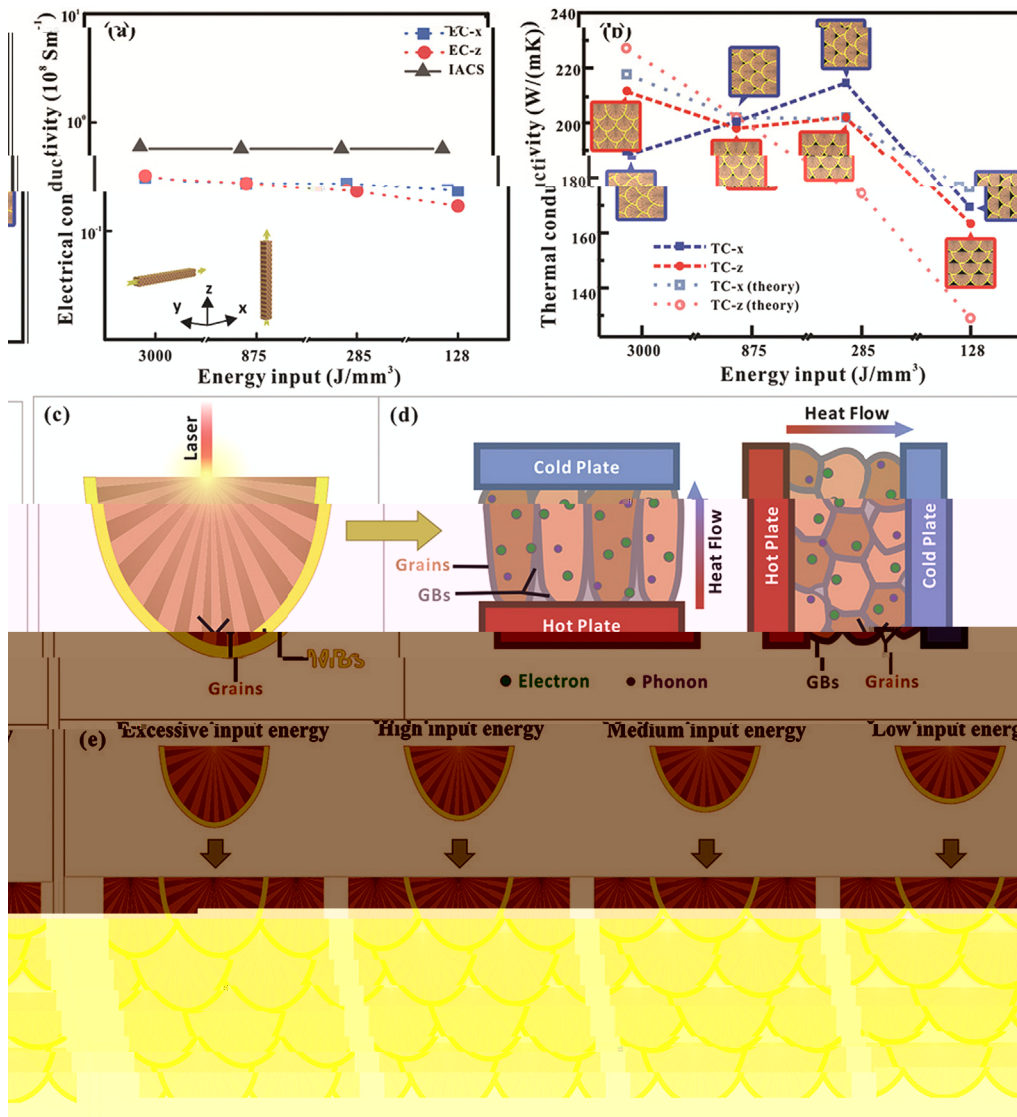


Fig. 7. (a) Electrical conductivity vs energy input; (b) Thermal conductivity vs energy input; (c) Schematic of laser heating; (d) Schematic of heat flow; (e) Schematic of grain growth under different energy inputs.

is very important for the design of the material.

3.3. Morphology and structure of CVD 3DG/Cu porous scaffolds

The porous scaffolds with different densities were fabricated by the laser-assisted CVD process. The morphology and structure of the scaffolds were investigated by SEM. As shown in Fig. 8a, the scaffolds have a porous structure with interconnected struts. The pore size is about 450 μm. The scaffolds were fabricated by the laser-assisted CVD process. The morphology and structure of the scaffolds were investigated by SEM. As shown in Fig. 8a, the scaffolds have a porous structure with interconnected struts. The pore size is about 450 μm. The scaffolds were fabricated by the laser-assisted CVD process. The morphology and structure of the scaffolds were investigated by SEM. As shown in Fig. 8a, the scaffolds have a porous structure with interconnected struts. The pore size is about 450 μm.

At the same time, the morphology and structure of the scaffolds were investigated by SEM. As shown in Fig. 8a, the scaffolds have a porous structure with interconnected struts. The pore size is about 450 μm. The scaffolds were fabricated by the laser-assisted CVD process. The morphology and structure of the scaffolds were investigated by SEM. As shown in Fig. 8a, the scaffolds have a porous structure with interconnected struts. The pore size is about 450 μm. The scaffolds were fabricated by the laser-assisted CVD process. The morphology and structure of the scaffolds were investigated by SEM. As shown in Fig. 8a, the scaffolds have a porous structure with interconnected struts. The pore size is about 450 μm.

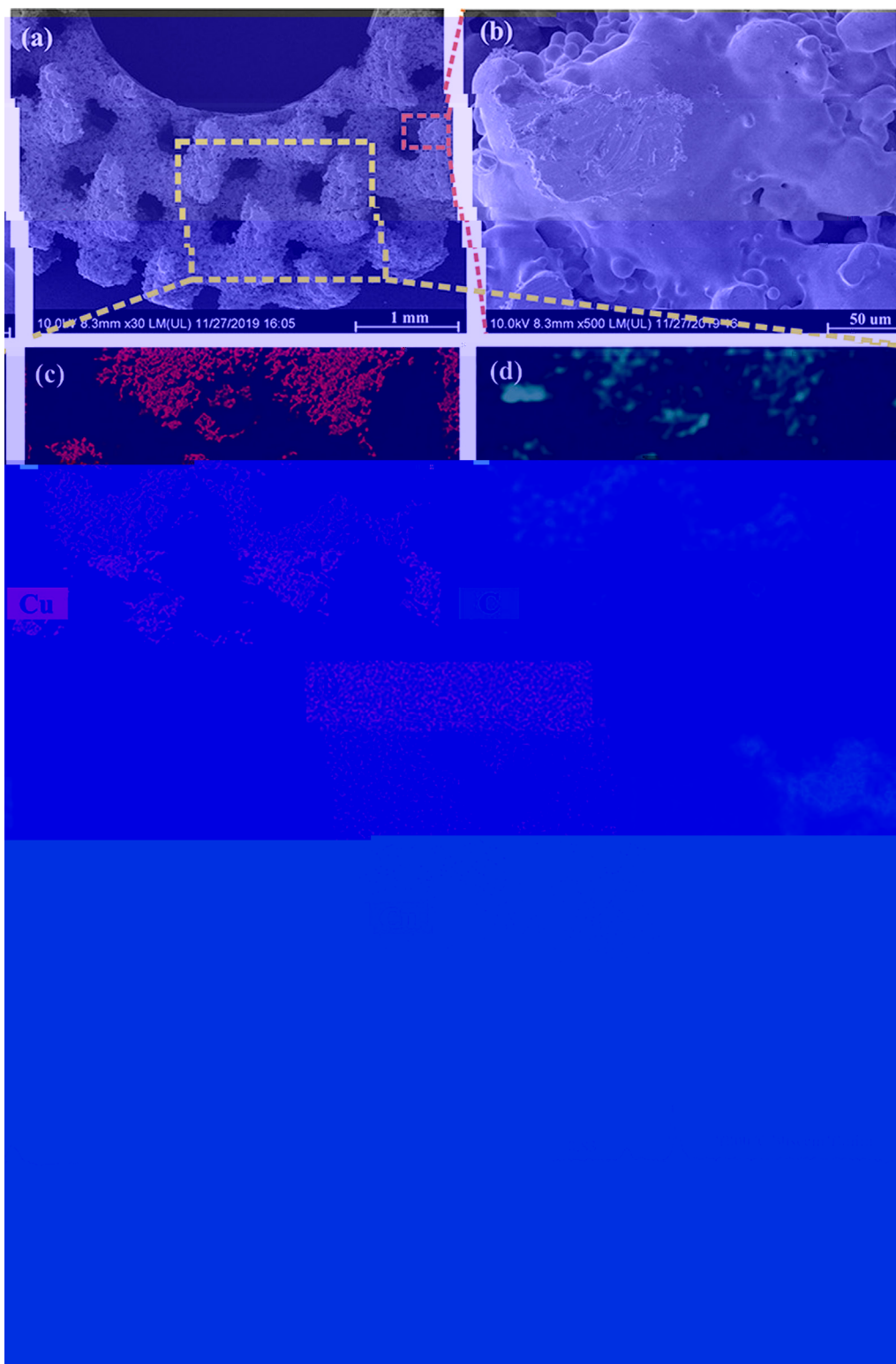


Fig. 8. (a) SEM image of 3DG/C porous scaffold; (b) Magnified SEM image of the scaffold surface; (c) EDS elemental map of C; (d) EDS elemental map of O; (e) EDS elemental map of Cu. The red dashed box in (a) indicates the region shown in (b).

The density of foams was measured by the Archimedes method. The density of foams was calculated by the following equation: $\rho = \frac{m}{V}$, where ρ is the density of foams, m is the mass of foams, and V is the volume of foams. As shown in Fig. 8, the porous scaffold (a) was prepared by the sintering of 3DG/C porous scaffold at 1000 °C, for 30 s, in a CH₄ atmosphere.

3.4. Thermal property and EMI shielding effectiveness of 3DG/Cu porous scaffolds

The thermal stability of 3DG/Cu porous scaffolds was evaluated by TGA. The TGA curves of 3DG/Cu porous scaffolds are shown in Fig. 9. The weight loss of 3DG/Cu porous scaffolds was 26.8% at 500 °C and 14.8% at 1000 °C.

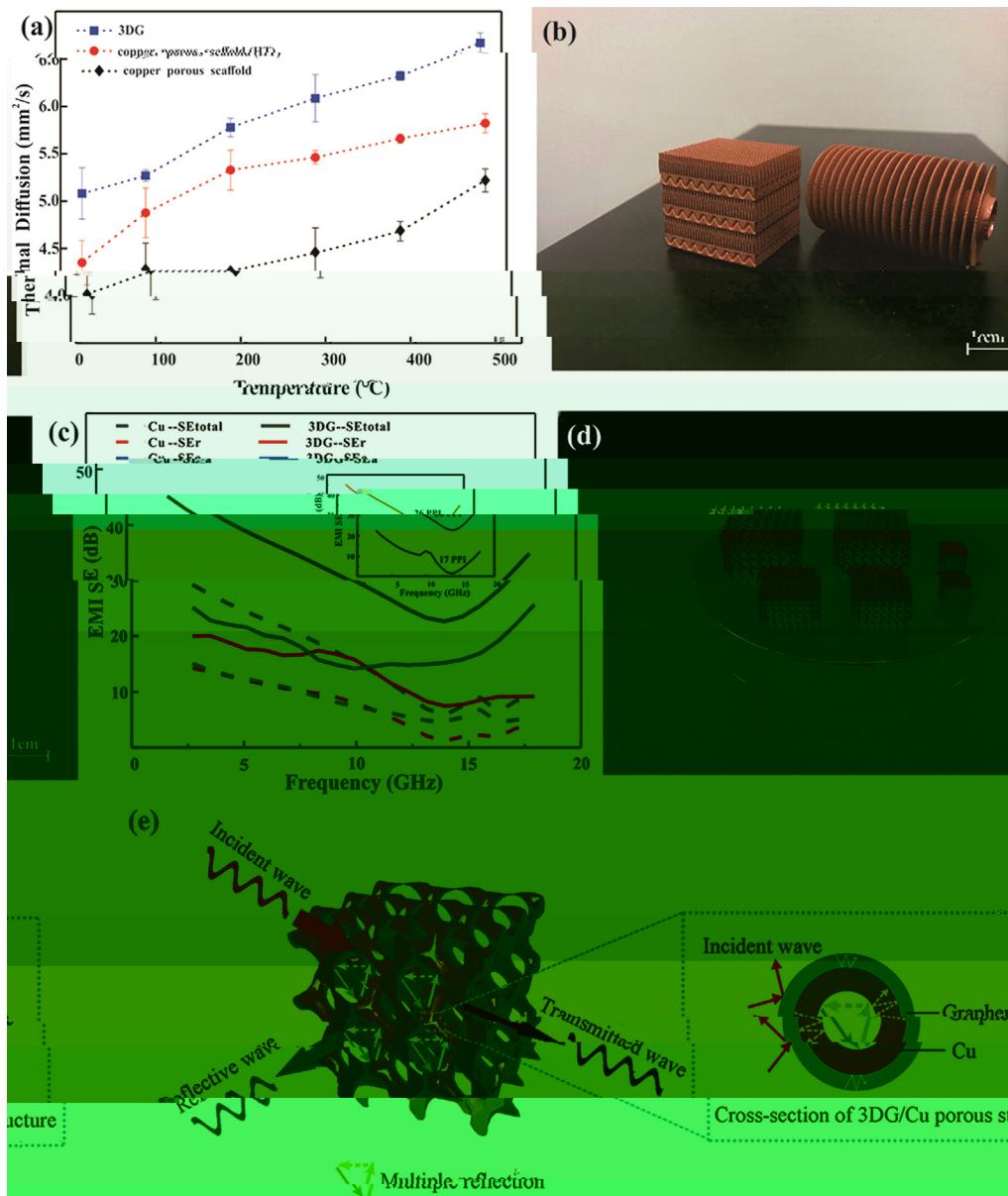


Fig. 9. Performance of 3DG/C porous scaffold: (a) thermal diffusion coefficient; (b) SLM prepared porous scaffold structure; (c) EMI SE; (d) porous scaffold structure; (e) Schematic of 3DG/C porous scaffold EMI SE. (For interpretation of the references to colour in this figure legend, the reader is referred to the web version of this article.)

Table 1

Comparison of the maximum shielding efficiency and improvement of thermal property for various porous structures.

| Coating materials | Substrate | Method | Maximum shielding efficiency (dB) | Improvement of thermal property (%) | Ref |
|-------------------|-----------|--|-----------------------------------|-------------------------------------|-----------|
| G | Al | Infiltration + sintering + CVD | 37 | - | 50] |
| G | PS | Hierarchical porous structure + sintering | 29.3 | - | 56] |
| G | PMMA | Sintering + infiltration + sintering + CVD | 19 | - | 57] |
| C /G | /C | Sintering + infiltration + CVD | - | 8.5 | 58] |
| G | Ni | Fabrication + CVD | - | 554 | 59] |
| G | C-Ni | Electroless plating + infiltration + sintering | 20 | - | 60] |
| G | C | Precipitation + CVD | - | 2.4 | 61] |
| G | Al | Fabrication + sintering | 47 | 6.3 | 62] |
| G | C | CVD + SLM | 47.8 | 27 | This work |

Note: Poly (ethylene terephthalate)-PPMA, polystyrene-PS.

test HT results were compared with the results obtained *in-situ* (Fig. 9a). Significant differences were observed between the two test methods. The SEM image of the HT result shows a clear interface between the fiber and matrix. The SEM image of the *in-situ* result shows a clear interface between the fiber and matrix. The SEM image of the *in-situ* result shows a clear interface between the fiber and matrix.

The stress-strain curves of the 3DG/C composites are shown in Fig. 9b. The SEM image shows the fracture surface of the 3DG/C composite. The SEM image shows the fracture surface of the 3DG/C composite.

The SEM image shows the fracture surface of the 3DG/C composite. The SEM image shows the fracture surface of the 3DG/C composite. The SEM image shows the fracture surface of the 3DG/C composite.

The SEM image shows the fracture surface of the 3DG/C composite. The SEM image shows the fracture surface of the 3DG/C composite. The SEM image shows the fracture surface of the 3DG/C composite.

4. Conclusions

At the 3DG/C interface, significant differences were observed between the two test methods. The SEM image shows the fracture surface of the 3DG/C composite. The SEM image shows the fracture surface of the 3DG/C composite.

Credit authorship contribution statement

Kaka Cheng: Conceptualization, Methodology, Formal analysis, Writing - review & editing. Wei Xiong: Visualization, Writing - review & editing. Yan Li: Writing - review & editing. Liang Hao: Formal analysis. Chunze Yan: Formal analysis. Zhaoqing Li: Visualization. Zhufeng Liu: Formal analysis. Yushen Wang: Investigation. Soft computing. Khamis Essa: Writing - review & editing. Li Lee: Data curation. Xin Gong: Software. Ton Peijs: Writing - review & editing, Supervision.

Declaration of Competing Interest

The authors declare that they have no competing interest.

Acknowledgement

This work was supported by the National Natural Science Foundation of China (No. 51671091, No. 51902295, No. 51675496). The authors thank the staff of the University of Georgia (UGA) (No. CUG170677) and the National Natural Science Foundation of China (No. 2019 CFB264).

Appendix A. Supplementary data

Supplementary data associated with this article can be found at <https://doi.org/10.1016/j.jpc.2020.105904>.

References

- Birg, N., N. M. T. K., M. S. G. (2018); 91:24–69.
- Birg, N., A. G. S., B. W., C. L. T., D. M. F., T. J. S. (2008); 8(3):902–7.
- Li, H., C. S. M., P. J. H., P. O., S. T. J., G. T. J. I. S. (2016); 8(36):24112–22.
- K. M., K. J., J. B. C., K. J. H., A. J. H. G. (2017); 11(8):7950–7.
- P. C., M. H. M., T. M., L. D. P. (2020); 262:118266–76.
- Li, X., W. C. L., J. S. H., W. G., L. J. F. (2017); 101:50–8.
- H. Q., L. S. W., C. L. H., J. S. H., H. Q. S. (2018); 6(42):21216–24.
- D. T. M., S. T. P., D. T. P., K. T. J., K. M. A. S. T., J. L. 3D (2017); 1(4):467–70.
- Q. L., L. L. T., S. L. P., S. L. P., S. L. P., S. L. P. (2014); 4(72):38273–80.
- D. X., H. L. S. P., N. W. J. G. 3D (2016); 90:424–32.
- Li, X., W. C. Q., H. M. K., X. H. L., D. W., T. J. S. (2018). <https://doi.org/10.1002/f.201803938>.
- Li, J. P., X. C. R., G., N. T. S. D., T. J. G. (2013); 7(7):6001–6.
- J. S. H., A. J. S. G. A. L. E. (2017); 56:15520–38.
- Ite, T., S. K., K. S. M., T. S. T., T. K., T. L. T. (2018); 20(9):6024–33.
- S. K., D. N., M. J. C., V. S. J. N., E. J. T. (2002); 149(8):370–7.
- C. X. H., S. M., S. W. H., L. G. H., X. Q., T. J. P. (2011); 7(22):3163–8.
- K. S. H., G. M., J. S. L., H. J. W., C. C. M. U. (2019); 1(4):1077–87.
- S. Q., F. X., L. W., L. H., L. T. J. C. (2017); 29(31):1701583–90.
- X. X., G. C., X. L., T. H., D. W., T. J. T. (2019). <https://doi.org/10.1021/s.9.08191>.
- C. C. H., B. X., N. J., C. S., L. F., T. J. 3D (2019); 175:107824–33.
- St.čić, B., Žić, D. T. (2016); 307:407–17.
- R. D., H. B., L. J., L. S. J., J. W., R. T. J. M. (2020); 771:138586–95.
- Li, X., C. W., A. J., K. S., N. J., D., T. J. L. (2009); 324(5932):1312–4.
- C. P., R. W. C., G. L. B., L. B. L., P. S. E., C. H. M. T. (2011); 10:424–8.
- J. S. D., D. S. S., G. S. S., L. K. T. J. P., H. J. V., V. S. J. K. (2019); 270:47–58.
- X. W., H. L., L. T., D. C. Q., F., T. J. E. F. (2019); 170:107697–708.
- G. D., M. S. W., W. K., P. R. L. S. (2013); 57(3):133–64.
- Li, E., T. S. C., S. L. F., T. A. E. F. (2017); 249:255–63.
- X. S., W. S., W. L., J. W. P., C., T. J. F. (2018); 124:685–98.
- Li, M. S., D. W., S. C. I. (2015); 87:797–806.
- L. C. L. A., M. S. S., T. M., A. T. R. C., W. S. P. J., L. P. D. T. (2019); 166:294–305.
- T. X., K., T. W. Q., T. J. D., S. S. M., M. J. D., T. J. R. (2016); 6:6039–48.
- K. H., T. X. P., L. N. H., T. S. B., C. K. G. (2016); 11(3):183–91.
- R. H. K., K. T. N. V., G. H., S. T. L., S. B. E. M. (2013); 22(12):3872–83.
- T. X., K., T. J. V., S. G. P. Q. X., G., T. J. A. (2015); 646:303–9.
- R. D. A., M. L. E., M. T. H., T. J. N. (2011); 59(10):4088–99.
- X., W. H. E. F. (2018); 743:258–61.
- K. S. W. L. T. Y. S. E. (2003); 23:309–48.
- L. G. S. T. J. F. Y. R., G. S. N. T. P. E. (2010); 10(9):3512–6.
- Li, X., C. W. W., C. L. R. E. F. R. E. Y. S. E. (2009); 9(12):4268–72.
- X. W., X. C., X. W. H., L. S. Q., L. A. S. J. (2020); 161:479–85.
- F. A. C., M. Y. J. C., S. V., C. S. C., L. M., M. F., T. J. R. (2006); 97(18):187401–4.
- S., G., J. S. H., F. P. C., H. Q. F. (2017); 200:97–100.
- J. K., H., J. C. J., D. F. L. T. E. (2014); 311:351–6.
- R. J. K., M. J. D. P., A. S. C., M. S., S. K. E. (2018); 12:475–84.
- S. B., L., W. C. S. J. (2016); 8(12):8050–7.
- L. N., H., D. F., H. X., L. X., G. O. (2018); 2-281.8(LJ0)-3(A)-340.5(S 54);

Mt 2019;34(5):489–98.

53] W B, C M, L M. R. *Journal of Materials Science: Part B: Physics of Condensed Matter* 2014;26:3484–9.

54] C H, W S, J J, X C, J J, et al. Synthesis of Fe₃O₄ Nanoparticles by Sol-gel Method. *Composites Part A* 2019;121:139–48.

55] W L, J, Q. T. *Journal of Materials Science: Part B: Physics of Condensed Matter* 2015;26(3):1895–9.

56] D X, P GR, H P, Q F, M B, et al. ML Efficiently Predicts the Mechanical Properties of Polymers. *Journal of Materials Chemistry C* 2012;22:18772–4.

57] H B, Q, W G, H X, et al. *Journal of Materials Chemistry A* 2011;3:918–24.

58] S A, U N, T V. T. *Journal of Materials Science: Part B: Physics of Condensed Matter* 2016. <https://doi.org/10.1051/comp/2016021>.

59] P M, J H, R S, S L. T. *Journal of Materials Science: Part B: Physics of Condensed Matter* 2012;12:2959–64.

60] J K, H H, D P. *Journal of Materials Science: Part B: Physics of Condensed Matter* 2017;122:244–7.

61] R H, L S, B S, K T, W L, D S, L H, et al. *Journal of Materials Science: Part B: Physics of Condensed Matter* 2015. <https://doi.org/10.1038/s12710-015-0127-1>.

62] X T, F S, G L, G Q, L G, R K, et al. *Journal of Materials Science: Part B: Physics of Condensed Matter* 2020. <https://doi.org/10.1016/j.jmbs.2019.105670>.

63] R D, M L, M E, H D, M J, M B, et al. *Journal of Materials Science: Part B: Physics of Condensed Matter* 2011;59(10):4088–99.

64] E S, F L, K C, S V, M C. T. *Journal of Materials Science: Part B: Physics of Condensed Matter* 1973;1(1):10–38.